Received: 26 July 2023 | Revised: 18 February 2024 | Accepted: 11 May 2024

DOI: 10.1002/jex2.158

RESEARCH ARTICLE

Mechanical property estimation of sarcoma-relevant extracellular vesicles using transmission electron microscopy

Premanshu Kumar Singh[1] | **Patricia Sarchet**[2] | **Catherine Hord**[3] | **Lucia Casadei**[2] | **Raphael Pollock**[2] | **Shaurya Prakash**[1,2]

[1]Department of Mechanical and Aerospace Engineering, The Ohio State University, Columbus, Ohio, USA

[2]Comprehensive Cancer Center, The Ohio State University, Columbus, Ohio, USA

[3]Center for Life Sciences Education, The Ohio State University, Columbus, Ohio, USA

Correspondence
Shaurya Prakash, Department of Mechanical and Aerospace Engineering, The Ohio State University, Columbus, Ohio, USA. Email: prakash.31@osu.edu

Funding information
DOD Peer Reviewed Cancer Research Program, Grant/Award Number: CA210874

Abstract

Analysis of single extracellular vesicles (EVs) has the potential to yield valuable label-free information on their morphological structure, biomarkers and therapeutic targets, though such analysis is hindered by the lack of reliable and quantitative measurements of the mechanical properties of these compliant nanoscale particles. The technical challenge in mechanical property measurements arises from the existing tools and methods that offer limited throughput, and the reported elastic moduli range over several orders of magnitude. Here, we report on a flow-based method complemented by transmission electron microscopy (TEM) imaging to provide a high throughput, whole EV deformation analysis for estimating the mechanical properties of liposarcoma-derived EVs as a function of their size. Our study includes extracting morphological data of EVs from a large dataset of 432 TEM images, with images containing single to multiple EVs, and implementing the thin-shell deformation theory. We estimated the elastic modulus, $E = 0.16 \pm 0.02$ MPa (mean±SE) for small EVs (sEVs; 30–150 nm) and $E = 0.17 \pm 0.03$ MPa (mean±SE) for large EVs (*l*EVs; >150 nm). To our knowledge, this is the first report on the mechanical property estimation of LPS-derived EVs and has the potential to establish a relationship between EV size and EV mechanical properties.

KEYWORDS
elastic modulus, extracellular vesicles, flow, liposarcoma, transmission electron microscopy

1 | INTRODUCTION

Soft tissue sarcomas (STS) are tumours that originate from mesenchymal cells and can occur anywhere in the body (Abeshouse et al., 2017; Gamboa et al., 2020; Thway, 2009). There are over 100 different sub-types of STS, with liposarcoma (LPS) being the most common, comprising up to 20% of all malignant cases (Brennan et al., 2014). The majority of patients with metastatic soft tissue sarcoma show a median survival rate of <1 year (Karavasilis et al., 2008). Liposarcomas are further classified into four sub-types based on histology and biological factors: well-differentiated (WDLPS), de-differentiated (DDLPS), myxoid and pleomorphic; among which WDLPS and DDLPS are most prevalent (Lee et al., 2018). The primary therapeutic intervention for LPS is surgery, which along with adjuvant treatment, still shows that more than half the patients develop recurrent or metastatic disease (Tan et al., 2016). LPS remains a lethal cancer for which we lack the means to unequivocally detect recurrence early when a cure may still be possible *via* therapeutic intervention (Anaja et al., 2009). Early detection of LPS recurrence is challenging as radiologic scans lack specificity, necessitating image-directed or open tissue biopsy resulting in time delays, significant costs and patient discomfort. Alternatively, a liquid biopsy is minimally invasive but requires a specific and reliable biomarker.

In the quest to find these biomarkers, extracellular vesicles (EVs) which are nanoscale structures made of a lipid bilayer secreted by nearly all cells have found a key niche (Phillips et al., 2021; van Niel et al., 2018). EVs contain DNA, RNA, and protein cargoes and are therefore promising structures to analyse (Elzanowska et al., 2021; Kalluri & LeBleu, 2020) for biomarkers. With the growing understanding of the role of EVs in communication between tumours and their surroundings, the potential involvement of EV contents in the initiation, progression and spread of cancer has also been hypothesised (Dixson et al., 2023; Mathieu et al., 2019; Tao & Guo, 2020; van Niel et al., 2022). Moreover, as previously reported, EVs are a rich biomarker source because the lipid layers protect EV cargo from enzymatic destruction in contrast to the analysis of cell-free circulating components (Casadei et al., 2021; Lazaro-Ibanez et al., 2019).

Previously, we reported an innovative, resource-efficient, three-dimensional microfluidic-nanofluidic device to isolate and capture LPS-derived EVs (Casadei et al., 2021). In this device, we reported that the LPS-derived EV cargo was not damaged during the mechanical pressure-driven microfiltration process to isolate EVs with a nearly 5-fold increase in the EV-cargo accessibility compared to standard methods such as ultracentrifugation (Casadei et al., 2021). Similar to our report, others have also reported on isolating EVs using microfluidics or other methods that subject EVs to mechanical forces as summarised in a recent review (Singh et al., 2022). Notably, the use of mechanical forces to filter EVs in order to obtain EV-enriched media is now a widely used approach (Chernyshev et al., 2022; Liang et al., 2017; Wang et al., 2013). Previous reports have also noted the deformation of EVs during these mechanical processing steps (Liu et al., 2022).

It is noteworthy that EVs are formed through multiple mechanisms as previously reviewed (Teng & Fussenegger, 2021). The classical view is that the biogenesis of small EVs (<150 nm in accordance with the *Minimum Information for Studies of Extracellular Vesicles* 2023 (MISEV 2023) guidelines (Welsh et al., 2024)) is through the endosomal pathway *via* invagination of the plasma membrane (Bebelman et al., 2018; Teng & Fussenegger, 2021). On the other hand, it is believed that the large EVs (>150 nm in accordance with the MISEV 2023 guidelines) are derived from the plasma membrane by direct outward budding and fusion, similar to endocytosis (Bebelman et al., 2018; Teng & Fussenegger, 2021). Given the distinct pathways for the biogenesis and secretion of EVs, we hypothesised that the structure and mechanical properties of the EVs would be size-dependent. Indeed, for example, past work with malignant and non-malignant exosomes from bladder cells showed that the malignant metastatic exosomes were nearly three times stiffer than the malignant but non-metastatic exosomes (Whitehead et al., 2015). Both types of malignant exosomes were significantly less stiff than the non-malignant exosomes (Whitehead et al., 2015). By contrast, for LPS, there are no reports that have evaluated the mechanical properties of the EVs. Knowing the biophysical properties of various EV sub-populations is important for the development of novel isolation methods that can potentially use size, deformability and/or shape as a means for EV separation and capture. To create effective therapeutic tools, it is imperative to have a comprehensive understanding of the biophysical properties required to develop stable and biocompatible nanocontainers that possess advanced functional, recognition and sensing abilities similar to EVs. Consequently, as the development of EV technologies for biomarkers (Lane et al., 2019; Tertel et al., 2022; Zhang et al., 2023) and therapeutics (Jung et al., 2022; Nguyen et al., 2022; Wiklander et al., 2019) continues, there is a need to better understand the mechanical properties of the EVs.

Conventional micromechanical techniques such as atomic force microscopy (AFM) have been extensively used for the measurement of the mechanical properties of EVs (Calo et al., 2014; LeClaire, Gimzewski et al., 2021; Royo et al., 2019; Sorkin et al., 2018). These techniques estimate the EV stiffness by fitting a Hertzian contact model to force-indentation curves (Chang et al., 2014). The assumptions used in Hertzian contact models may not be suitable for EVs, particularly for small EVs, and accurately describing the mechanical response of these vesicles in the linear regime can be difficult (Vorselen et al., 2017). Additionally, the inherent adhesion, hard substrate effects, and the immobilisation of EVs on the substrate make AFM problematic for softer EVs. AFM measurements also lack high-throughput and are therefore limited to a small number of EVs that are analysed in each sample (Parisse et al., 2017). To address these challenges, recent efforts by Ridolfi et al. (2020) have introduced a high-throughput AFM-based approach for the nanomechanical screening of single EVs. Despite these advancements, the diverse range of elastic moduli reported for EVs still spans nearly three orders of magnitude, underscoring the need for alternative methods. In this context, microfluidics coupled with optical imaging has been explored to estimate the mechanical properties of larger apoptotic bodies (1–5 μm) (Rodriguez-Quijada & Dahl, 2021). Techniques like real-time deformability cytometry have been developed which use a similar flow-based methodology to determine the mechanical stiffness of cells (Mietke et al., 2015; Peng et al., 2011). However, no such alternate method for smaller EVs exists.

In this paper, we present a first report on the mechanical property estimation of the LPS-derived EVs. We use the flow-derived, post-filtration EVs representative of microfiltration in our previously reported microfluidic-nanofluidic device. The microfiltration process was combined with transmission electron microscopy imaging to quantify the change in shape during filtration. This change in shape is evaluated using well-established principles of thin-shell theory to estimate the elastic modulus for the EVs. Consequently, we report on the distribution of EV size, EV-membrane thickness and present comparative images from patient-derived EVs. Therefore, the purpose of this paper is to provide the first report on detailed visualisation and mechanical characterisation of LPS-relevant EVs using a whole-EV deformation analysis through transmission electron microscopy imaging.

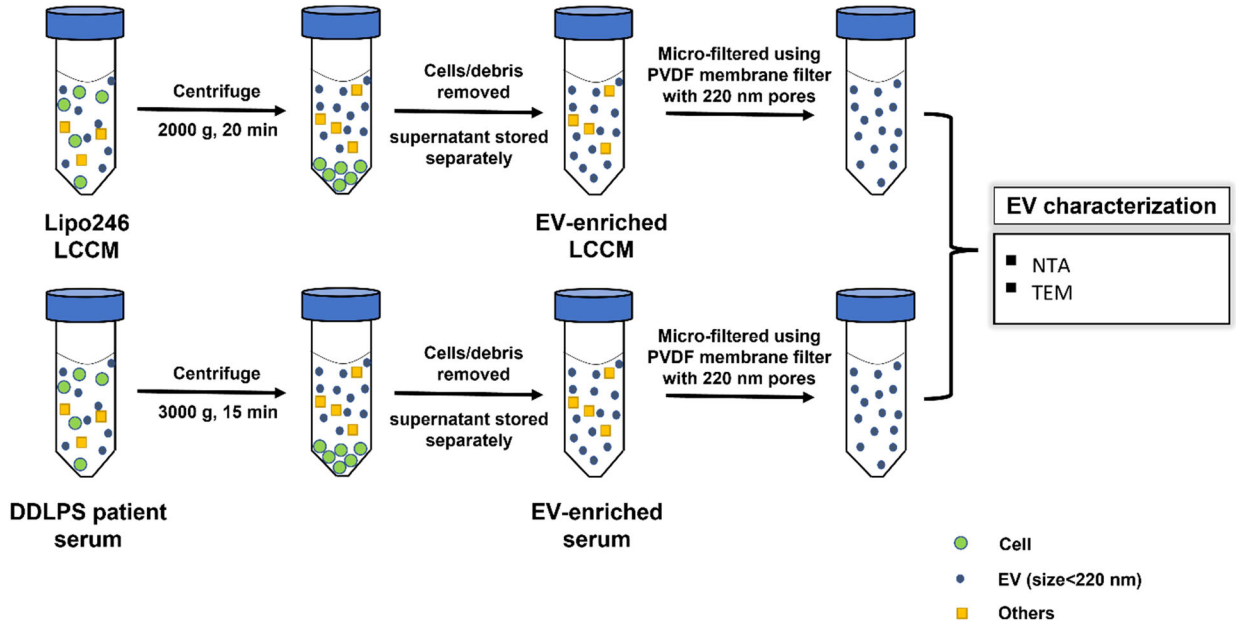

FIGURE 1 EV processing and analysis. Schematic depicting the process to generate EV-enriched LCCM and DDLPS patient serum for analysis of EVs to obtain mechanical properties. NTA, nanoparticle tracking analysis; TEM, transmission electron microscopy.

2 | MATERIALS AND METHODS

2.1 | Cell culture

We used the previously established human LPS cell line Lipo246 (Peng et al., 2011). Maintained at standard conditions, the cells were grown in Dulbecco's Modified Eagle Medium (DMEM; Gibco) and supplemented with 10% (vol/vol) Fetal Bovine Serum (FBS). Cells were serum-starved with serum-free DMEM for 48 h for EV production and Lipo246 cell line conditioned media (LCCM) was subsequently collected. LCCM was centrifuged (Eppendorf Centrifuge 5810 R) at 2000 *g* for 20 min before further use.

2.2 | Patients and clinical samples

LPS patient blood samples were collected at The Ohio State University James Cancer Medical Centre. Following the Helsinki Declaration under the auspices of a protocol (Protocol number: 2014C0028) approved by The Ohio State University James Cancer Medical Centre Institutional Review Board, written informed consent was received from the participants before inclusion in the study. Vacutainer Serum Separation Tubes (BD Scientific) were used to collect the patient venous blood. Whole blood samples were centrifuged (Eppendorf Centrifuge 5810 R) at 1900 *g* for 10 min at 4°C, and the retrieved blood serum was aliquoted and stored at -80°C until further analysis. Any residual cells and debris were removed from the serum by centrifuging at 3000 *g* for 15 min.

2.3 | Microfiltration of EVs from LCCM and DDLPS patient serum

Figure 1 shows schematically the process for the microfiltration of EVs from LCCM and DDLPS patient serum reflecting the mechanical forces seen by the biofluids during sample preparation and operation of the microfluidic device, reported previously (Casadei et al., 2021). Specifically, the frozen samples at −80°C were thawed at 4°C for 1 h. For use of the LCCM, post-thawing, 1.7 mL of media was microfiltered using PVDF membrane syringe filters (Tisch Scientific) at a flow rate of 0.1 mL/s. The pore size and effective filtration area of these membranes as provided by the manufacturer were 220 nm and 4.9 cm^2, respectively. After the filtration, the microfiltered media was collected into an Eppendorf tube and stored at −80°C until further use. A similar protocol was followed for the microfiltration of DDLPS patient serum. All the experiments were carried out in triplicates.

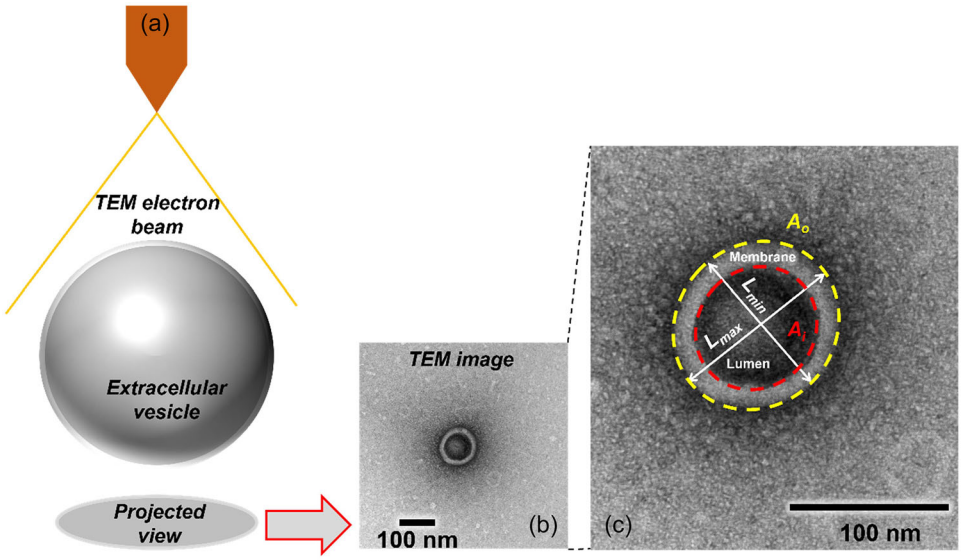

FIGURE 2 Transmission electron microscopy. (a) Experimental schematic showing acquisition of TEM micrographs for the EVs. (b) Representative TEM image of an EV. (c) Zoomed in image acquired for the extracellular vesicle (EV) shown in (b). The dashed yellow and red lines represent the fitted geometries for shape analysis to evaluate EV deformation. The membrane and lumen extent are labelled as L_{min} and L_{max} denoting the major and minor axis assuming the fit geometry to be an ellipse. A_i and A_o, respectively denote the area of the inner and outer fitted ellipse.

2.4 | Characterisation of LCCM-derived EVs

2.4.1 | Transmission electron microscopy

7.5 μL of LCCM was placed on a glow discharged formvar coated and carbon stabilised copper grid (Electron Microscopy Sciences, Hartfield, PA) at room temperature. After 20 mins, the TEM grid was washed with phosphate buffer (pH = 7.4) twice, and 7.5 μL of 1:1 solution of phosphate buffer (pH = 7.4) and 2.5% glutaraldehyde was placed on the grid for 5 mins at room temperature. The grid was rinsed with DI water three times and immediately stained with 1% (w/v) uranyl-acetate in ethanol for 30 s. The grid was then air-dried after manually removing any excess liquid with blotting paper. Transmission electron microscopy images were obtained using a FEI Tecnai G2 Spirit microscope (80 kV accelerating potential), at The Ohio State University Campus Microscopy & Imaging Facility (CMIF). ImageJ (v1.44) was used to post-process the micrographs.

2.4.2 | Nanoparticle tracking analysis

Nanoparticle tracking analysis (NTA; Malvern NanoSight NS300) was used to quantify the size distribution and concentration of EVs in conditioned media similar to previous reports (Casadei et al., 2019; Casadei et al., 2021; Casadei et al., 2022). Using the MISEV 2023 guidelines (Welsh et al., 2024), small EVs (sEVs; 30–150 nm) and large EVs (*l*EVs; > 150 nm) were classified for reporting results. We note that in the LPS-relevant EVs evaluated in this paper, we see distinct differences in EV characteristics with an approximate size cut-off of 120 nm. Therefore, whilst this article follows the MISEV 2023 guidelines for sEVs and *l*EVs, we also note our observations with respect to the size of the LPS-relevant EVs.

2.4.3 | EV size and morphological analysis from TEM micrographs

ImageJ (v1.44) was used for extracting the size and morphology of the EVs from TEM micrographs. As seen in Figure 2b, TEM micrographs revealed particles with an electron-dense lumen (cargo) surrounded by a membrane bilayer. Only vesicles with visible membrane bilayer or a cup-shaped morphology or those similar to other accepted TEM visualisations (Broad et al., 2023; Rikkert et al., 2019) of the EVs were included for the shape and elastic property analysis. Each TEM micrograph was fitted with an outer and an inner ellipse of best fit (Figure 2c), and the area enclosed by the outer ellipse of best fit (A_o in Figure 2c) was used for calculating the size of the EV with the diameter denoted by D_o using Equation (1) (White, 2011). Similarly, the area of the inner ellipse of best fit (A_i) was used to calculate the size of the lumen (D_i) using Equation (2) (White, 2011). The uncertainties are reported to account for error in fitting the geometrical shape to the EV images. Using over 400 images, many with multiple

EVs in each image provides reasonable statistics for the validation of the imaging method reported here to obtain an estimate of the EV elastic modulus.

$$D_o = \sqrt{\frac{4A_o}{\pi}}, \tag{1}$$

$$D_i = \sqrt{\frac{4A_i}{\pi}}. \tag{2}$$

The shape of the projected image of the EV was characterised by the eccentricity of the outer fitted ellipse, using Equation (3) (Ayoub, 2003), where L_{max} and L_{min} are the major and minor axes of the fitted ellipse (as represented in Figure 2c). An eccentricity, $\varepsilon = 0$ corresponds to a spherical vesicle, and $\varepsilon = 1$ corresponds to an elongated (i.e., rod-shaped) vesicle. The lipid membrane thickness, t of the EV was calculated by Equation (4).

$$\text{Eccentricity} \quad (\varepsilon) = \sqrt{1 - \frac{L_{min}^2}{L_{max}^2}}, \tag{3}$$

$$\text{Membrane thickness} \quad (t) = \frac{D_o - D_i}{2}. \tag{4}$$

2.4.4 | TEM-based size analysis to complement NTA size observations

The TEM micrographs of the LCCM-derived EVs revealed particles of varying size with a near-spherical shape with an electron-dense lumen (cargo) surrounded by a membrane bilayer (Figure 2b,c). All the pre- and post-filtered triplicates were imaged and a total of 432 TEM images with one or multiple EVs were analysed for the LCCM-media, with 107 images from pre-filtered LCCM samples and 325 images were from post-filtered LCCM samples. EVs in the size range of 10–280 nm were observed in the TEM micrographs of pre-filtered media samples. EVs in size range of 10–953 nm were observed in the TEM micrographs of post-filtered LCCM samples. These TEM micrographs were used to analyse the dependence of EV size on its shape (eccentricity, ε) and lipid bilayer membrane thickness (t). Moreover, the EV lipid bilayer membrane thickness-to-size ratio is referred to as membrane thickness ratio (MTR) and defined by Equation (5).

$$\text{Membrane thickness ratio} \quad (MTR) = \frac{t}{D_o} \tag{5}$$

The Full Width at Half Maximum (FWHM) for each of the significant NTA peaks was calculated. Subsequently, the EVs were grouped to the FWHM sizes after TEM imaging, within size ranges defined by the NTA peak ± FWHM/2. The FWHM is a statistical metric (Smith, 2003) used to express the width of a curve or function at the point where its value is equal to half of its peak or maximum value.

2.4.5 | Estimation of elastic modulus

Thin shell theory (ŁUkasiewicz, 1971; Sanders, 1963; Seide & Nordgren, 1976; Timoshenko & Woinowsky-krieger, 1959) was adopted for the mechanical modelling of EVs. Notably, thin-shell theory has found utility in prior studies for modelling the mechanical behaviour of diverse biological particles, encompassing cells (Mietke et al., 2015) and viral capsids (Roos et al., 2010). Additionally, thin-shell theory has been employed for indentation modelling of EVs in atomic force microscopy (AFM) analysis (LeClaire, Gimzewski et al. 2021; Royo et al., 2019; Whitehead et al., 2015). According to this theory, an EV is assumed to mechanically behave as a hollow shell with thin wall thickness with respect to its size, and a non-zero elastic modulus (E). The elastic modulus used to mechanically characterize EVs in this study is an intrinsic property which is a measure of the relationship of stress and strain in the linear elasticity region of the deformation along a single axis (LeClaire, Gimzewski et al., 2021). Given our past work has shown that mechanical filtration does not damage the LPS-cargo inside the EV (Casadei et al., 2021), and the range of observed MTR, thin-shell theory is one viable option to estimate E. Furthermore, no bending of the EV was assumed under uniform loading, which represents a force to deform the entire EV during mechanical filtration. Therefore, the

radial deformation of the EVs in the axisymmetric planar flow is then used to estimate the elastic modulus, E as defined by Equation (6) (Timoshenko & Woinowsky-krieger, 1959):

$$E = (1-\upsilon)\frac{D_o^2 \Delta p}{8wt}. \quad (6)$$

In Equation (6), E is the elastic modulus of the EV in Pa, υ is the Poisson ratio of EV, D is the size of the EV in m, Δp is the average pressure-difference driving micro-filtration through the syringe filter in Pa, t is the membrane thickness in m and w is the radial deformation due to micro-filtration in m. The analytical deformation modelling of the thin-shelled EV is illustrated in Figure S2. Additional details on the model and equations used are available in the Supplementary material (section 1.2). Equation (6) requires a reasonably accurate estimation of the average pressure drop (Δp) across the filtration membrane which was obtained using a COMSOL Multiphysics model similar to past work (Casadei et al., 2021). The Δp obtained from the COMSOL model was experimentally validated by using the flow rate from the filtration experiment to yield an experimental Δp by Darcy's law (Darcy, 1856). Experimental results and the COMSOL model agreed within 0.79% with the average Δp obtained from the COMSOL model being 16.47 kPa and the experimental measurement yielding a pressure drop of 16.34 kPa.

Briefly, a three-dimensional (3D) computational domain (Figure S1) was modelled to simulate the micro-filtration of the EVs across the PVDF membrane. The detailed numerical model is included in the Supplementary material (section 1.1). The control volume with the flow across the PVDF membrane was modelled to reduce the computational burden. The PVDF membrane was modelled as a porous medium with an effective filtration area of 4.9 cm^2 and pore size of 220 nm as obtained from the manufacturer's datasheet. The permeability (κ) of the membrane was calculated using the Carman-Kozeny equation (Carman, 1937; Carman, 1997; Kozeny, 1927). A constant fully developed mass flow rate boundary condition was implemented at the membrane inlet and the membrane outlet was open to the atmosphere. All governing equations were solved under the assumptions of steady-state, incompressible and isothermal flow conditions (Rangharajan et al., 2016). The Brinkman equation (Durlofsky & Brady, 1987) was used to solve for the flow in the porous PVDF membrane. The simulated results were re-iterated until mesh-insensitive solutions were attained with a numerical tolerance of the converged solution at 10^{-5}.

2.5 | Data analysis and statistics

Statistical analysis was performed using JMP 16 (SAS Institute Inc., Cary, NC, 1989–2021). Continuous variables were described as bar charts with overlapped data points, whose upper line represented the mean, and the error bar represented the standard deviation in the positive direction. The distribution of continuous variables between different groups was compared using non-parametric Kruskal-Wallis and Mann-Whitney tests for pairwise comparisons which do not assume sample normality or equal variances assumptions (Fay & Proschan, 2010). All statistical tests were two-sided and conducted at a significance level, $\alpha = 0.05$. Figures showing statistical data analysis were prepared using OriginPro (OriginLab Corporation, Northampton, MA, USA; Version 2022b).

3 | RESULTS

3.1 | Microfiltration of LCCM

LCCM was microfiltered using a PVDF filter with a pore size of 220 nm. This process was executed to mimic the filtration procedure employed in our microfluidic-nanofluidic device (Casadei et al., 2021). The primary objective was to target the clinically relevant size range of LPS-derived EVs (Casadei et al., 2021; Casadei et al., 2022) and LPS patient serum (Figure S4) indicates that LPS-relevant EVs are generally <200 nm. Using past work for DDLPS serum and Lipo246 cell line derived EVs (Casadei et al., 2019; Casadei et al., 2022), biological characterisation of EVs has been previously reported to confirm the enrichment of EVs from the conditioned media. Figure 3a shows the size distribution of particles in the pre-filtered LCCM with dominant contributions from the EVs with a size of 57.5, 70.5, 193.5 and 320.5 nm as quantified by the NTA measurement. The particle fraction in NTA-quantified size distribution plots is defined as the ratio of particle concentration of a given size to the number of total particles in the sample. Figure 3b,c shows the *MTR* and EV ε respectively. Both *MTR* and ε were obtained from the TEM micrographs for the EVs in the size ranges: 57.5 ± 4.9 nm, 70.5 ± 10 nm and 193.5 ± 52.7 nm, where each size range is NTA peak ± FWHM/2. The representative TEM micrographs of EVs in Figure 3 are shown in Figure 4. No EVs were observed by the TEM in the size range of 320.5 ± 14 nm.

The NTA characterisation of post-filtered media showed a higher heterogeneity in EV size, consistent with past reports (Casadei et al., 2021; Dehghani et al., 2019). Multiple size peaks as measured by NTA (Figure 5) were observed at 43.5, 71.5,

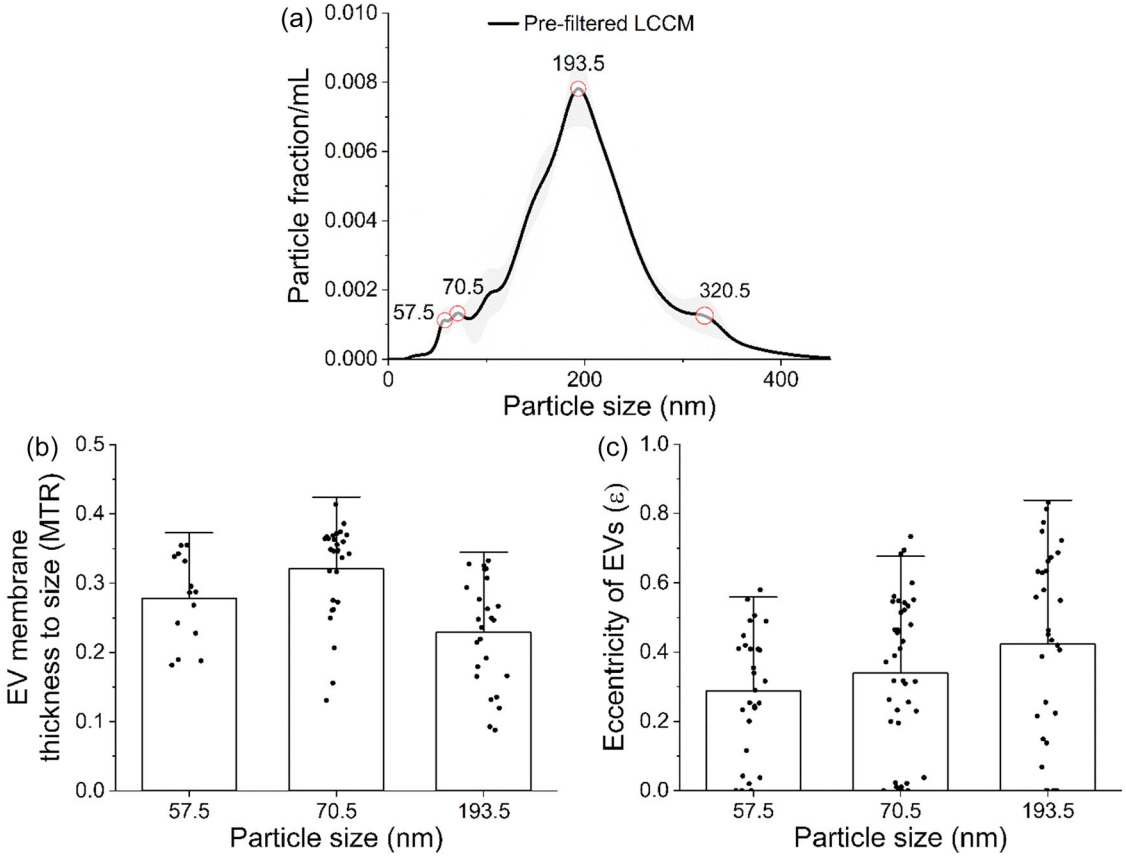

FIGURE 3 NTA of pre-filtration LCCM. (a) Shows the nanoparticle size tracking assay summary with the main sizes identified in the conditioned media. (b) Shows a distribution of the *MTR* for the key sizes of the EVs (<220 nm). (c) represents the eccentricity of the EVs. EVs were assumed to be spherical based on existing literature. Therefore, any observations of non-spherical EVs were quantified as a non-zero eccentricity, with eccentricity of 1 indicating an elongated rod-shaped EV. The figure shows distribution of the EVs prior to filtration and confirms the TEM observations that EVs may not necessarily be spherical. Error bars are + standard deviation.

86.5, 119.5, 164.5, 202.5, 257.5, 292.5 and 348.5 nm. The representative TEM micrographs for these NTA peaks are shown in Figure 6. Like the pre-filtered NTA, FWHM was calculated for these dominant particle sizes in the post-filtered media. Figure 5b shows the distributions for the *MTR*. The $0.1 < MTR < 0.4$ remains relatively consistent for EVs ≤ 120 nm in size. As the EV size increased to nearly 350 nm, the *MTR* range changed to $0.08 < MTR < 0.2$. Therefore, this data suggests that the larger EVs (>120 nm) present thinner outer membranes compared to the EVs with mean size ≤120 nm for the LPS-relevant vesicles. Similarly, Figure 5c demonstrated that the $\varepsilon \sim 0.5$ for EV size ≤ 120 nm and approached $\varepsilon \sim 0.6$ for EVs with size >120 nm.

Figure 7a shows that *MTR* of sEVs in the pre-filtered LCCM has a mean of 0.28 with a range of ~ 0.1 to 0.4. Similarly, for *l*EVs, *MTR* was noted to have a mean value of 0.23 with a distribution range observed from 0.1 to 0.33. Post-filtration (Figure 7b), a similar *MTR* comparison showed that sEV mean was 0.25 within the range of 0.1–0.4 and *l*EVs showed a mean of 0.1 with the range varying from 0.03 to 0.22, with a few outliers. Therefore, these nanoscale particles can be approximated as thin shells where the outer enclosure is thin with respect to the overall size (ŁUkasiewicz, 1971; Sanders, 1963; Seide & Nordgren, 1976; Timoshenko & Woinowsky-krieger, 1959).

3.2 | Evaluating change in shape of EVs due to microfiltration

The ε of EVs were also assessed pre- and post-filtration. ε for sEVs was noted to increase from 0.38 to 0.50 ($p < 0.0001$; Figure 8a) and for *l*EVs an increase from 0.4 to nearly 0.7 ($p < 0.001$; Figure 8b). It is worth noting that the range of ε values spans a variety of shapes from nearly perfect spheres ($\varepsilon = 0$) to largely elliptical and approaching a perfect rod-like shape ($\varepsilon = 1$) as visualised using TEM imaging and quantified in Figure 8 for both pre- and post-filtration. Figure S7 illustrates the change in the shape of the EVs post microfiltration.

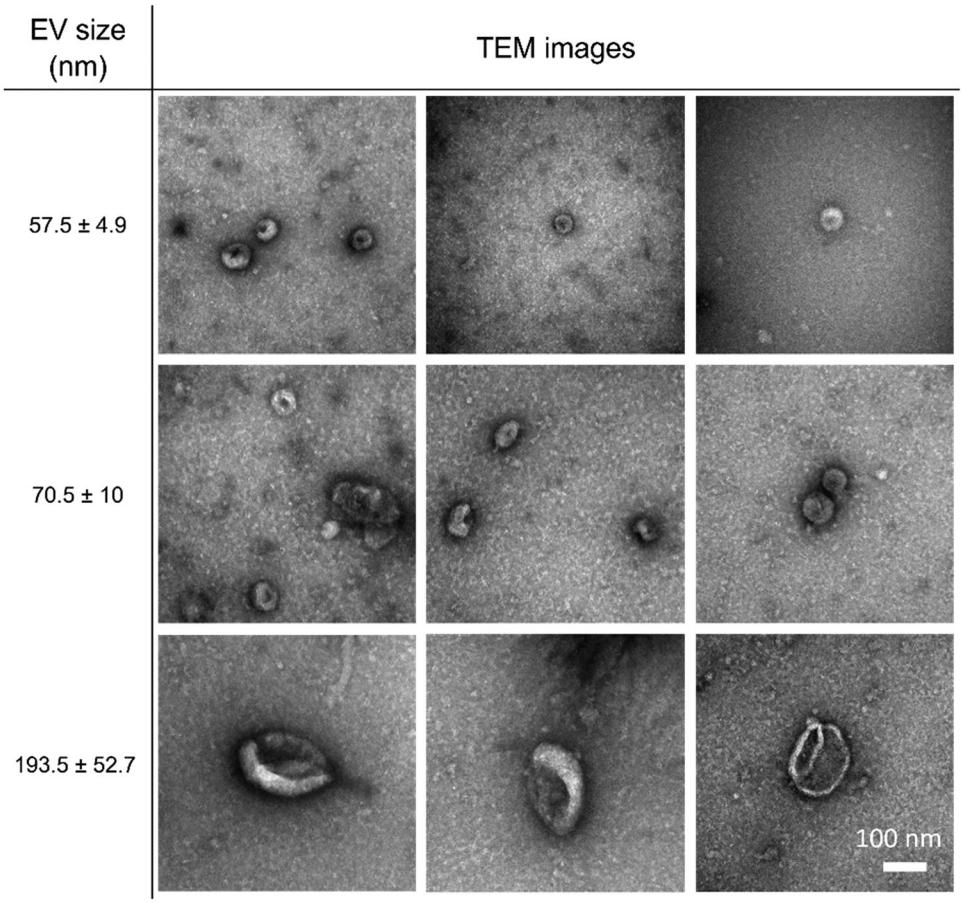

FIGURE 4 Imaging. Representative TEM images of EVs derived from LCCM prior to mechanical filtration.

3.3 | Elastic modulus of liposarcoma EVs

As noted above for Figure 7, the EVs present a reasonable approximation to the well-established thin shell deformation theory (Seide and Nordgren, 1976; Timoshenko and Woinowsky-krieger, 1959). Therefore, using Equation (6) the elastic modulus of these EVs was calculated. It was found that the elastic modulus (E) yielded $E = 0.16 \pm 0.02$ MPa (mean ± standard error) for sEVs and $E = 0.17 \pm 0.03$ MPa (mean ± standard error) for *l*EVs, as shown in Figure 9. Despite the noted differences in EV size and *MTR*, the difference in the calculated E for sEVs compared to *l*EVs was not statistically significant based on the image analysis from 432 TEM images.

3.4 | Characterisation of DDLPS patient serum

LCCM provides a method to generate EVs in a controlled laboratory setting. To further elucidate the morphology of EVs for LPS, we present a first report on the detailed image-based observations of DDLPS patient serum in Figure 10. Additionally, Figure S4A,B report the size distribution of the serum pre- and post-filtration (using 220 nm pore size PVDF filters) measured *via* NTA. Like the particle distributions observed for the LCCM, multiple dominant sizes were observed. For pre-filtered serum, the major EV sizes were observed at 113.5, 178.5, 201.5 and 279.5 nm. Once again, increased size heterogeneity was noted for post-filtered serum with dominant sizes noted at 105.5, 117.5, 194.5 and 321.5 nm.

Interestingly, whilst imaging the DDLPS patient serum *via* TEM, images show sEVs (<100 nm) are dominant with the larger EVs not easily imaged. Moreover, TEM-imaging of DDLPS patient serum also shows a significant presence of electron-dense particles without a visible lipid bilayer (Figure 10a), which most likely represent lipoproteins in pre-filtered serum. The sEVs (Figure 10b–d) with a thick bilayer lipid membrane and the expected deflated cup shape, suggestive of EVs, were also observed. Figure 10b,c illustrates the wide-field and close-up images of EVs as recommended by MISEV 2023 (Welsh et al., 2024) guidelines. It is noteworthy that EVs for DDLPS serum may exist independent of other particles (Figure 10b,c) or these EVs were surrounded by smaller spherical structures (Figure 10d), similar to those previously reported in electron microscopic imaging of fresh plasma

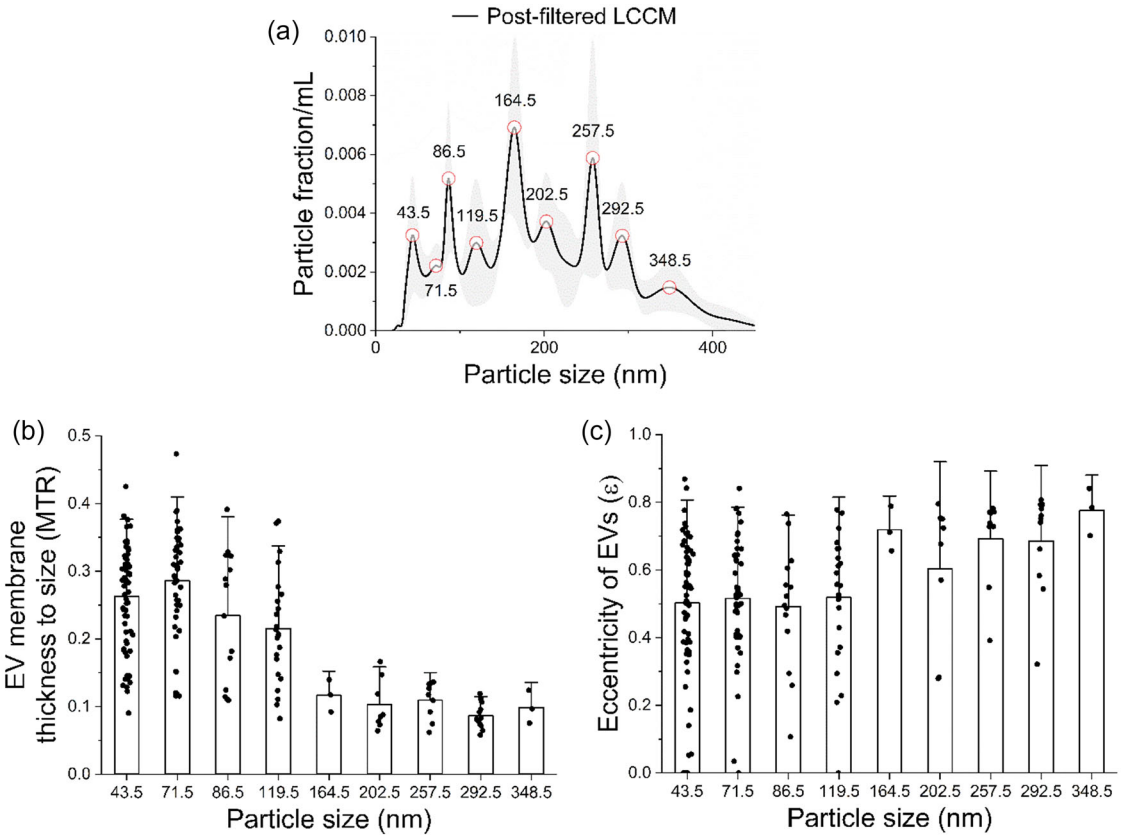

FIGURE 5 NTA of post-filtration LCCM. (a) Shows the nanoparticle size tracking assay summary with the main sizes identified in the conditioned media, post-filtration. (b) Shows a distribution of EV membrane thickness to EV size ratios for the key sizes of the EVs. (c) represents the eccentricity of the EVs. The ideal EV-shape was assumed to be spherical based on existing literature. Therefore, any observations of non-spherical EVs were quantified as a non-zero eccentricity, with perfect eccentricity of 1 indicating an ideal rod-shaped vesicle. Error bars are + standard deviation.

samples of healthy adults (Yuana et al., 2013) and THP-1 human monocytes-derived EVs (Yang et al., 2022). With no prior reports of EM-imaging of DDLPS patient serum-derived EVs, the observations here present the first in-depth look at visualising DDLPS EVs.

4 | DISCUSSION

It is now generally agreed that cells release a variety of EVs that show differing characteristics such as size, density, charge, protein expressions, and cargo composition (Phillips et al., 2021; Vagner et al., 2019), that is, EVs in biofluids comprise a highly heterogeneous collection of nanoparticles. The isolation, purity and subsequent characterisation of this heterogeneous population of EVs remains a challenging research problem with evolving standards and guidelines. For example, it has been shown that EV associated protein and miRNA from B16-F10 melanoma, 4T1 breast cancer, and Pan02 pancreatic cell lines were different (Zhang et al., 2018). Additionally, the heterogeneity between EVs has been noted to extend across both sEVs and *l*EVs (Haraszti et al., 2016; Phillips et al., 2021). However, for LPS, significant characterisation of the heterogeneity of the EVs is currently lacking. Therefore, in this paper we present one set of detailed mechanical characterisation of LPS-relevant EVs using NTA and TEM-based analysis to complement our previous reports that noted various advances in analysing the LPS-relevant EVs for biochemical composition with relevance to the use of *MDM2* DNA as a potential biomarker for sarcoma recurrence (Casadei et al., 2019; Casadei and Pollock, 2020; Casadei et al., 2022).

We provide an extensive TEM-imaging based characterisation of the LPS-relevant EVs. To our knowledge, this is the first and largest data set of TEM images used for the characterisation of LPS-relevant EVs. Notably, this work shows an innovative use of whole-EV deformation, representing the actual mechanical processing of EVs for isolation and to estimate the EV mechanical properties. The mechanical analysis is complemented by NTA to determine particle sizes. Furthermore, this data complements the past reports from our team that have characterised these EVs for their cargo and proteins (Casadei et al., 2019; Casadei et al., 2022) and also the use of innovative microfluidics for biomarker quantification from both LCCM and blood sera from 5

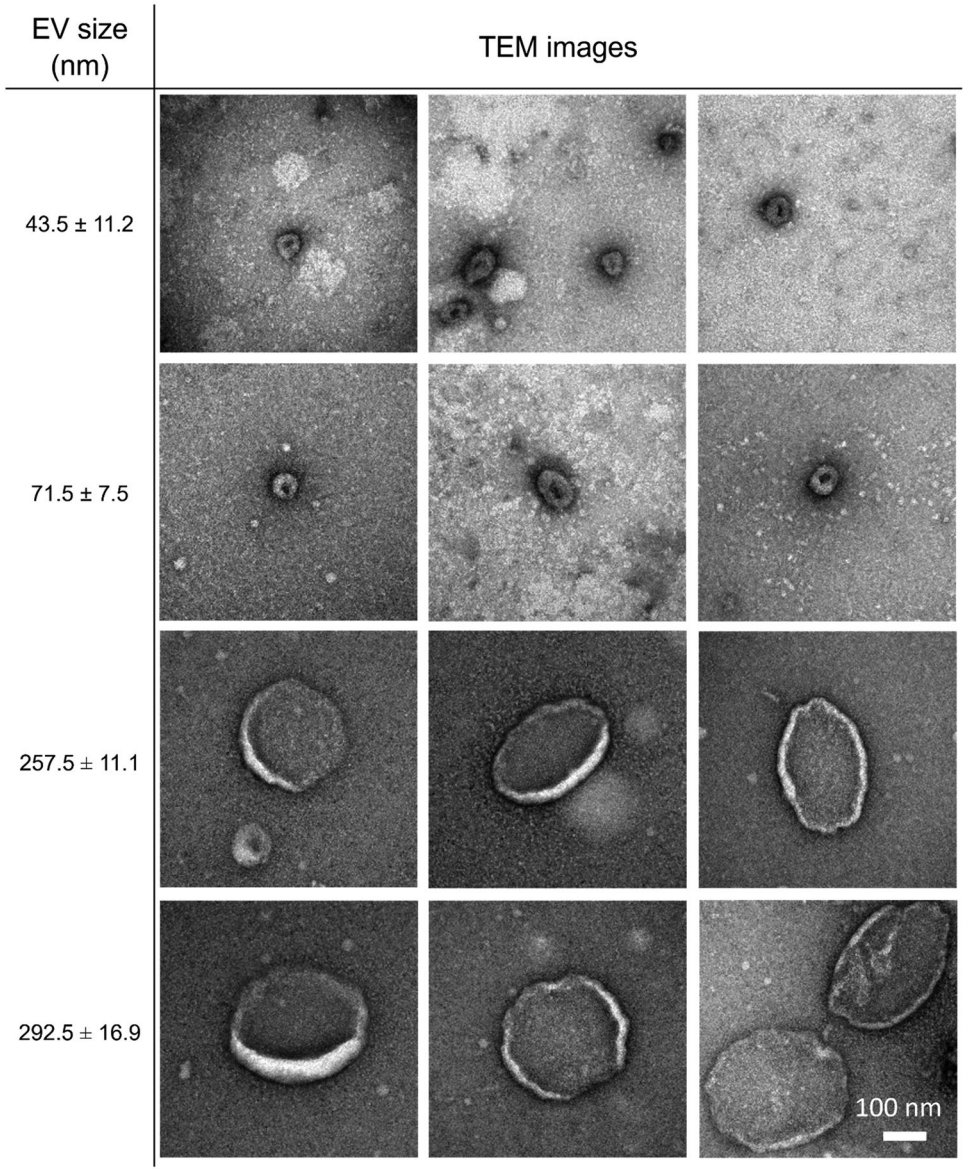

FIGURE 6 Imaging. Representative TEM images of EVs derived from LCCM post mechanical filtration. Additional TEM images of EVs with varied sizes are included in Figure S3.

DDLPS patients (Casadei et al., 2021). Here, in addition to the detailed mechanical analysis of the LCCM-derived EVs, we report additional visualisation of EVs from another DDLPS patient using TEM imaging for a rare and difficult to treat cancer.

The TEM analysis of LCCM-derived EVs was conducted on 432 high resolution TEM images to build a detailed data set complementing the standard size distribution analyses done through NTA measurements. The quality of the sample may be affected by the source of the EV, as the complex and viscous sources like patient sera are onerous to handle and can easily lead to EV coagulation and co-isolation of macro-molecular constituents (Li et al., 2023; Yuana et al., 2015).

Microfiltration was carried out for three different samples and the average particle concentrations were reported in Figures 3a and 5a. It is noteworthy that post-microfiltration the polydispersity in the LCCM for the observed EV sizes increased from the relatively more monodisperse composition. Size-based filtration narrows the observation window to select sizes and the NTA measurement likely amplifies the sizes that may not be observed as relative concentrations as in unfiltered samples. Past work has also observed similar changes to the particle size distributions (Dehghani et al., 2019) with the reasons attributed to filter heterogeneity, non-uniform filter compositions, deformation of EVs, and agglomeration (Chernyshev et al., 2022; Merchant et al., 2010). It is important to note that only particles with EV cup-shaped morphology were used for the mechanical property analysis. We show in Figure S5 the likely images of non-EV materials such as lipoproteins or other aggregates that would be seen in the NTA analysis but are not taken into account during the mechanical property analysis.

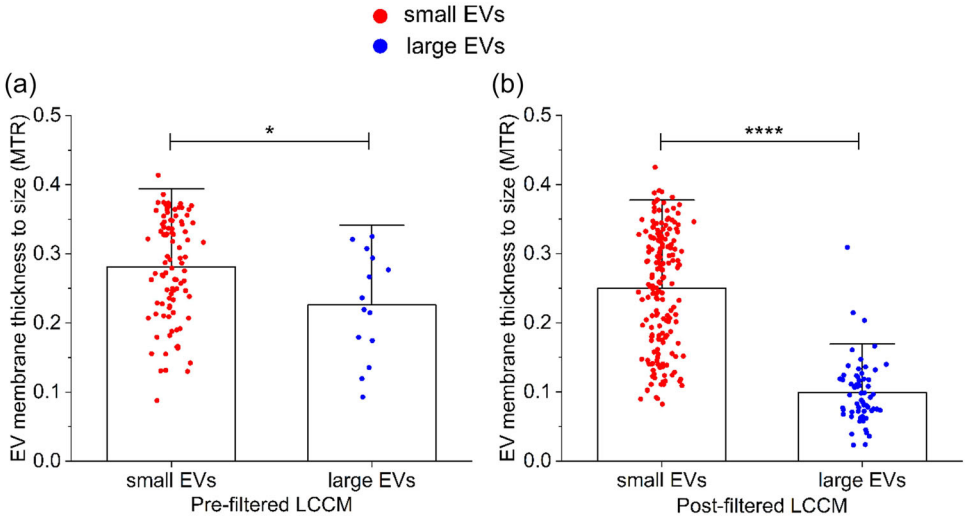

FIGURE 7 MTR comparisons. Comparison of the *MTR* between sEVs and *l*EVs in (a) pre-filtered and (b) post-filtered LCCM. The reported *MTR* values for EVs in pre-filtered LCCM (a) were 0.23 ± 0.05 for sEVs and 0.28 ± 0.05 for *l*EVs. In post-filtered LCCM (b), our reported MTR values were 0.25 ± 0.08 for sEVs and 0.11 ± 0.05 for *l*EVs. * signifies $p < 0.05$ and **** signifies $p < 0.0001$. The sEV and *l*EV classification follows MISEV 2023 guidelines. Error bars are + standard deviation.

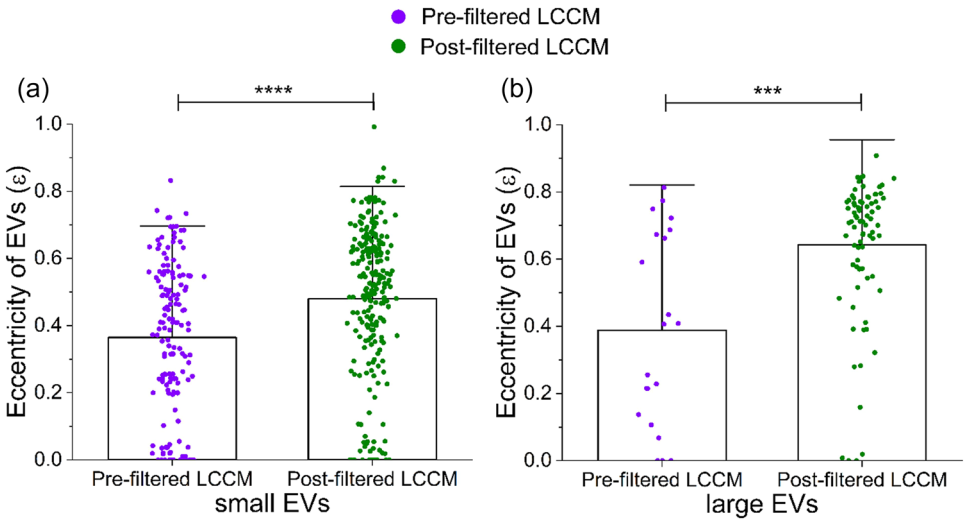

FIGURE 8 ε comparisons. Comparison of eccentricity of EVs between pre-filtration and post-filtration of LCCM for (a) sEVs and (b) *l*EVs. *** signifies $p < 0.001$ and **** signifies $p < 0.0001$. Error bars are + standard deviation.

There are limited studies in the literature which have reported mechanical properties of cancer derived EVs. For breast adenocarcinoma cell lines, LeClaire, Wohlschlegel et al. (2021) reported that the EVs (40–120 nm) obtained from highly metastatic MDA-MB-231 cells showed a lower average modulus ($E = 0.61 \pm 0.03$ MPa) compared to those obtained from low metastatic cells (MCF7 EVs, $E = 0.85 \pm 0.07$ MPa) and non-metastatic cells (MCF10A EVs, $E = 0.97 \pm 0.07$ MPa). In another report, the stiffness of exosomes derived from T24 cell line (Human malignant non-metastatic bladder carcinoma) and FL3 cell line (Human malignant metastatic bladder carcinoma) were noted to be 95 and 280 MPa, respectively (Whitehead et al., 2015). On the other hand, Zhang et al. (2018) reported $E = 145$–816 MPa for exomeres (~35 nm), $E = 70$–420 MPa for small exosomes (60–80 nm) and 26–73 MPa for large exosomes (90–120 nm) for EVs derived from B16-F10 mouse melanoma cell line, MDA-MB-4175 breast adenocarcinoma cell line, and AsPC-1 pancreatic ductal adenocarcinoma cell line, respectively. In yet another report, exosomes derived from a highly aggressive and metastatic k-ras-activated human osteosarcoma (OS) cell line (143B) showed $E \sim 192$ MPa which was more than the $E \sim 118$ MPa of exosomes derived from a non-aggressive and non-metastatic k-ras-wildtype human OS cell line, and a highly aggressive and metastatic murine OS cell line (LM8) which was reported to be $E \sim 111$ MPa (Yurtsever et al., 2021). Some reports have also published elastic modulus for synthetic and natural vesicles. For example, Calo et al. (2014) reported a high elastic modulus of ~300 MPa for plasma and inner membrane nanovesicles (~80 nm) obtained from

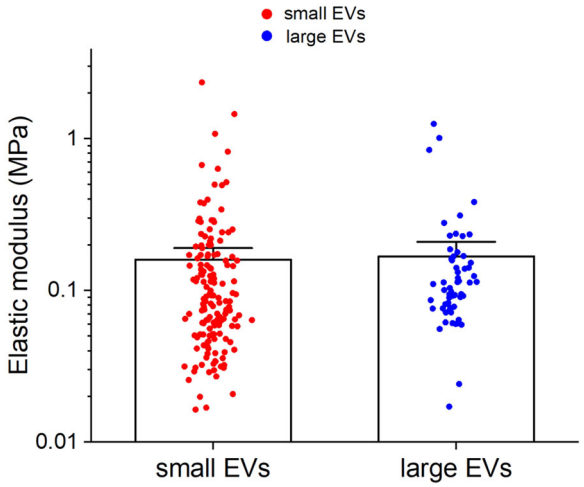

FIGURE 9 EV elastic modulus. The elastic modulus was estimated to be $E = 0.16 \pm 0.02$ MPa (mean ± SE) for sEVs (30–150 nm) and $E = 0.17 \pm 0.03$ MPa (mean±SE) *l*EVs (>150 nm). The modulus for EVs was calculated using the thin-shell theory. Error bars are + standard error.

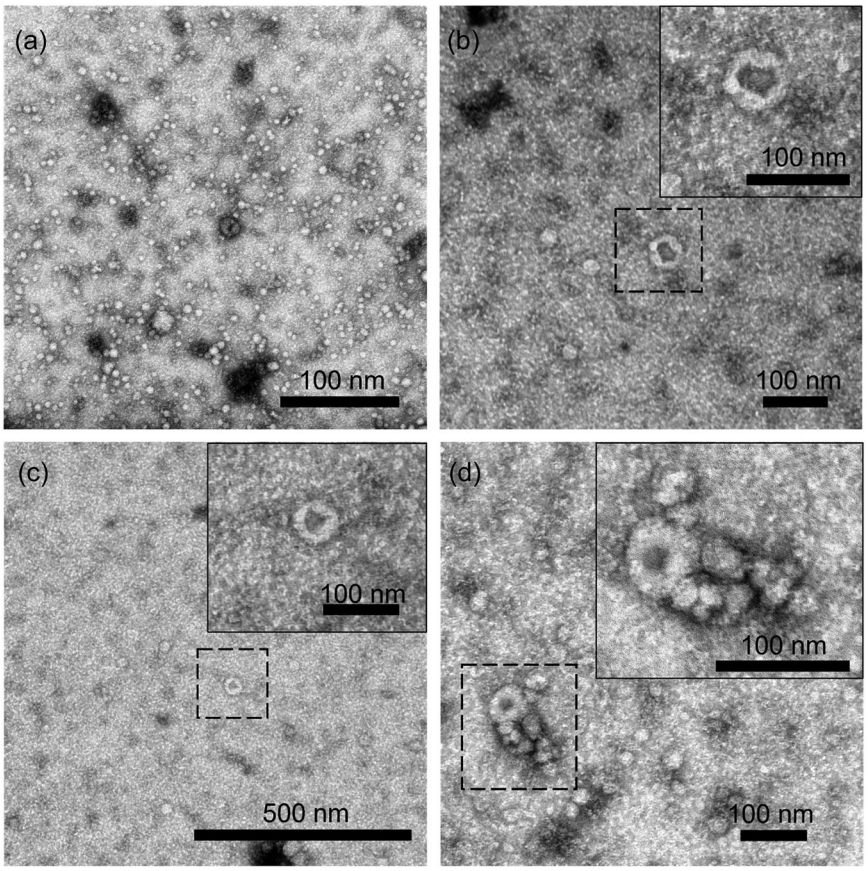

FIGURE 10 TEM imaging of post-filtered DDLPS patient serum. A highly heterogeneous set of particles were observed by TEM imaging in post-filtered patient serum. Electron-dense particles likely to be lipoprotein particles were observed frequently (a). Electron-dense particles with cup-shaped morphology representing likely EVs were also observed (b–d). Close-up images of EVs are included at the top right corner of (b), (c) and (d). Electron-dense vesicles surrounded by smaller spherical aggregates were also observed (d). The image presentation for serum follows the MISEV 2023 guidelines for sharing such data. These images are the first set of detailed TEM images for DDLPS patient serum.

disrupted yeast *Saccharomyces cerevisiae* cells. Elastic modulus for cholinergic synaptic vesicles were in the range of 0.2–13 MPa (Laney et al., 1997). In summary, the range of reported E values for EVs ranges from 0.2 to 420 MPa with no consensus on the mechanical properties either for specific cancers, EV-type, or EV-size.

We estimated the mean E for sEVs and *l*EVs to be $E = 0.16 \pm 0.02$ MPa and $E = 0.17 \pm 0.03$ MPa, respectively, which is closer to the lower bound of previously reported values. It is noteworthy that all the past studies utilised an atomic force microscope (AFM) for the measurement of E values. An AFM uses a sharp tip to induce nano-indentations at a single point on an EV for subsequent force-displacement analysis leading to the determination of the elastic modulus. Previously, it has been shown that the nano-indentation experiments result in the build-up of osmotic pressure difference within the vesicle due to the leakage of its contents

(water and possibly membrane solute permeable solutes), which in turn resists the indentation and thereby increases the apparent EV elastic modulus (Tang et al., 2020; Vorselen et al., 2017). Yet, an unresolved question persists whether EVs possess anisotropic or isotropic mechanical properties. This unresolved question assumes significance for the nano-indentation approach as the EV is subjected to a single-point load (or force) and a past report has noted that the calculated elastic modulus was dependent on the orientation of the immobilised EV on the substrate (Parisse et al., 2017). Furthermore, For AFM-based nano-indentation, the AFM tip, substrate and the EVs all present finite electrostatic charges with the subsequent effect of electrical interactions not completely understood (Zhang et al., 2018).

In this work, our approach used a microfiltration process that is similar to the actual filtration processes seen by EVs and the analysis approach uses a whole-EV deformation analysis based on the validity of the thin-shell assumption. As the data reported here shows, the EVs undergo deformation due to uniformly distributed pressure (~17 kPa) around the vesicles with no damage to the cargo (Casadei et al., 2021). It is important to highlight the fact that there are no established validation protocols for the mechanical analysis of such biological samples. Therefore, measuring the mechanical properties of soft nanoscale vesicles remains a challenging task that requires accuracy and precision.

The lipid bilayer membrane surrounding the lumen of EVs consists of an array of molecules such as lipids, proteins, nucleic acids, cholesterols, and glycans, which are integral and peripheral to the EV membrane (Hallal et al., 2022). These components collectively form an outer corona layer that envelops the EV membrane and can display as a brighter region or corona at the EV periphery (Cedervall et al., 2007; Tóth et al., 2021; Wolf et al., 2022). In this study, we used TEM micrographs of EVs to measure their membrane thickness, following the procedure outlined in Section 2.4.3. The resultant membrane thickness of EVs from the filtered sample (as illustrated in Figure S6) yielded measurements of 16.7 ± 7.5 nm (mean ± SD) for sEVs (30–150 nm) and 43.1 ± 31.9 nm (mean ± SD) for *l*EVs (>150 nm). Notably, our results tend towards the upper end of the range when compared to membrane thickness values reported in the existing literature (Calo et al., 2014; Perissinotto et al., 2021). The reported variation in membrane thickness may be influenced by the presence of the protein corona layer. In negatively stained TEM images, the corona layer is identified as dense staining around the EV indicating the presence of a filamentous halo, rendering the EV boundary notably thicker and more diffuse (Kesimer et al., 2009; Wolf et al., 2022). Kesimer et al. (2009) used TEM imaging to report the presence of a 10–30 nm thick coronal layer surrounding the exosomes derived from human tracheobronchial epithelial cells. Wolf et al. reported a corona layer of around 50 nm for nano-sized EVs derived from therapy-grade human placental-expanded stromal cells (Wolf et al., 2022). Wolf et al. (2022) also demonstrated a depletion in the corona layer following ultracentrifugation. However, our study found no significant change in corona layer thickness resulting from the filtration step employed, as depicted in Figure S8. This finding can be attributed to the lower mechanical pressure exerted on the EVs during filtration (~17 kPa) employed in this study, which is considerably less than that generated by methods like ultracentrifugation (~50 MPa) (Molina-Garcia, 1999). Thus, the EV deformation is attributed to the mechanical forces due to filtration as no change was observed in the outer layers of the EVs. Moreover, as shown previously (Casadei et al., 2021), the mechanical filtration through the 200 nm nanocapillary membrane does not damage the EV-cargo. We also note that the cup-shaped appearance of EVs is just one of the various representations of EVs observed through electron microscopy. Other studies have presented images of EVs resembling those we have depicted (Ridolfi et al., 2023; Rikkert et al., 2019), whilst others have shown multiple EVs connected or contained within one another (Broad et al., 2023; Morandi et al., 2022). Therefore, the use of electron microscopy for the visualisation of EVs remains a method in evolution as not all different forms of EVs have yet been completely imaged.

The molecules such as proteins, glycans, and cholesterols on the EV surface affect the stiffness of EV and control the movement of phospholipid molecules in the membrane (Hallal et al., 2022). Membrane rupture is avoided in the EVs during instances of local strain by the reorganisation of phospholipids of the membrane (Morshed et al., 2020). Variation in the biogenesis of EV sub-types (sEVs, *l*EVs, apoptotic bodies) gives rise to the difference in their membrane composition. For example, comprehensive lipidomic analyses of EVs from adipocytes and infrared spectroscopy analyses of EVs from Jurkat T-cells, prostate cancer cells, and melanoma cells revealed that the small (<100 nm), intermediate (100–450 nm), and large (>450 nm) EV sub-types have distinct lipid profiles (Durcin et al., 2017; Mihaly et al., 2017; Paolini et al., 2020). Similarly, the EV sub-type governs its surface protein composition (Belov et al., 2016; Castillo et al., 2018). The presence of cholesterols also influences the membrane stiffness (Waugh and Song, 1991) and membrane bilayer thickness as a consequence of its condensing effect in lipid bilayers (de Meyer and Smit, 2009; Hung et al., 2007).

Numerical studies using thermodynamic analyses have demonstrated that bilayer thickness and membrane stiffness play a crucial role in influencing the vesicle size distribution and configuration (Huang et al., 2017). Past theoretical research suggests that multiple physical schemes compete to regulate the physicomechanical properties of nanovesicles (i.e., EVs or similar particles between 20 and 200 nm in size) (Chng et al., 2021). The classic membrane model proposes that the effective stiffness of a nanovesicle increases exponentially with a decrease in vesicle size, because of entropic effects due to reduced thermal undulation and non-linear curvature elasticity effects (Ahmadpoor and Sharma, 2016; Helfrich, 1986; Hung et al., 2007). On the other hand, a past study reported nanovesicle softening with a decrease in vesicle size, attributed to the change in the bilayer's interior structure, i.e., a decrease in lipid packing with an increase in membrane curvature (Chng et al., 2021). Our results showed that sEVs exhibit a higher membrane thickness-to-size ratio compared to *l*EVs (Figure 7). Additionally, our whole-EV deformation analysis showed that there is no statistically significant difference in the mean elastic modulus between sEVs and *l*EVs. It is important to note

here that the size range for *l*EVs with EVs > 150 nm was much wider as compared to sEVs (30–150 nm). The variation observed in the elastic modulus data of EVs can be attributed to the uncertainty in the calculated pressure drop across the membrane, which in turn stems from manufacturing uncertainties in the material characteristics of the membrane. To thoroughly assess the variability in the average pressure drop, an uncertainty analysis was conducted. The manufacturer provided information on the membrane's characteristics, including an effective filtration area of 4.9 cm^2 and a nominal pore diameter of 220 nm. Based on a previous study on similar nanocapillary membranes (Vitarelli et al., 2011), the uncertainty in the membrane thickness was considered within a range of ±10%, whilst the uncertainty in the pore diameter was considered within a range of 0% to −20%. By incorporating these uncertainties into the analysis, the average pressure variability was determined to be ±54%. This range provides a measure of the potential variability in the pressure drop and facilitates a more reliable evaluation of the uncertainty in the elastic modulus of the EVs.

One of the limitations of the thin-shell model is that the model does not consider either the osmotic pressure across the EV membranes or the viscoelastic properties of the EV membranes. Despite the limitations of the thin-shell theory, the methodology provides a critical first step towards high throughput, whole EV deformation analysis. Future work can improve on this method by including viscoelastic properties of the EVs, which may necessitate the use and development of more complex models. Furthermore, it is important to note that the EV characterisation with NTA and TEM does not provide a one-to-one correlation between the NTA data and TEM imaging due to the distinct modalities of data acquisition and subsequent data reporting. As an optical measurement based on light scattering, NTA measures all particles regardless of composition or type (Comfort et al., 2021). On the other hand, TEM imaging is a region of interest (ROI) method that images a smaller area or volume of a sample (Rikkert et al., 2019). Therefore, for representative images, multiple images must be acquired. In this work, our analysis includes over 400 images of post-filtered media containing EVs, with many images containing multiple EVs allowing a broader statistical analysis with associated uncertainties being reported. In essence, this work extracts morphological and geometric data of EVs from TEM micrographs to estimate their mechanical properties.

5 | SUMMARY AND CONCLUSIONS

This is the first report on the mechanical property estimation of LPS-derived EVs. In this paper, a flow-based methodology complemented by electron microscopy is used to provide a high-throughput and whole EV deformation analysis for estimating the mechanical properties of EVs as a function of their size. Despite the observed variations in size and membrane to size ratio among sEVs and *l*EVs, the difference in calculated elastic modulus for sEVs and *l*EVs was statistically insignificant. We also observed a higher membrane thickness-to-size ratio for sEVs compared to *l*EVs.

AUTHOR CONTRIBUTIONS

Premanshu Kumar Singh: Conceptualisation (equal); data curation (lead); formal analysis (lead); investigation (lead); methodology (lead); project administration (supporting); resources (equal); software (lead); validation (lead); writing—original draft (lead); writing—review and editing (lead). **Patricia Sarchet**: Methodology (supporting); project administration (supporting); resources (equal); writing—review and editing (supporting). **Catherine Hord**: Data curation (supporting); formal analysis (supporting); writing—review and editing (supporting). **Lucia Casadei**: Methodology (supporting); resources (supporting); writing—review and editing (supporting). **Raphael Pollock**: Funding acquisition (equal); project administration (lead); resources (lead); supervision (lead); writing—original draft (supporting); writing—review and editing (supporting). **Shaurya Prakash**: Conceptualisation (supporting); funding acquisition (equal); project administration (lead); supervision (lead); writing—original draft (supporting); writing—review and editing (supporting).

ACKNOWLEDGEMENTS

The authors would like to acknowledge the instruments and services provided by The Ohio State University Comprehensive Cancer Centre (OSUCCC) Flow Cytometry Shared Resource for Nanoparticle Tracking Analysis (NTA). We also acknowledge resources from the Campus Microscopy and Imaging Facility (CMIF) and the OSUCCC Microscopy Shared Resource (MSR), The Ohio State University. This work was supported by DOD CDMRP Grant CA210874.

CONFLICT OF INTEREST STATEMENT

The authors declare no competing interests.

ORCID

Premanshu Kumar Singh https://orcid.org/0009-0001-6698-8694
Lucia Casadei https://orcid.org/0000-0002-5731-8197
Raphael Pollock https://orcid.org/0000-0002-0443-1583
Shaurya Prakash https://orcid.org/0000-0002-5263-0843

REFERENCES

Abeshouse, A., Adebamowo, C., Adebamowo, S. N., Akbani, R., Akeredolu, T., Ally, A., Anderson, M. L., Anur, P., Appelbaum, E. L., Armenia, J., Auman, J. T., Bailey, M. H., Baker, L., Balasundaram, M., Balu, S., Barthel, F. P., Bartlett, J., Baylin, S. B., Behera, M., … Zmuda, E. (2017). Comprehensive and integrated genomic characterization of adult soft tissue sarcomas. *Cell*, *171*, 950–965. e928.

Ahmadpoor, F., & Sharma, P. (2016). Thermal fluctuations of vesicles and nonlinear curvature elasticity-implications for size-dependent renormalized bending rigidity and vesicle size distribution. *Soft Matter*, *12*, 2523–2536.

Anaja, D. A., Lahat, G., Liu, J., Xing, Y., Cormier, J. N., Pisters, P. W., Lev, D. C., & Pollock, R. E. (2009). Multifocality in retroperitoneal sarcoma: A prognostic factor critical to surgical decision-making. *Annals of Surgery*, *249*, 137–142.

Ayoub, A. B. (2003). The eccentricity of a conic section. *The College Mathematics Journal*, *34*, 116–121.

Bebelman, M. P., Smit, M. J., Pegtel, D. M., & Baglio, S. R. (2018). Biogenesis and function of extracellular vesicles in cancer. *Pharmacology & Therapeutics*, *188*, 1–11.

Belov, L., Matic, K. J., Hallal, S., Best, O. G., Mulligan, S. P., & Christopherson, R. I. (2016). Extensive surface protein profiles of extracellular vesicles from cancer cells may provide diagnostic signatures from blood samples. *Journal of Extracellular Vesicles*, *5*, 25355.

Brennan, M. F., Antonescu, C. R., Moraco, N., & Singer, S. (2014). Lessons learned from the study of 10,000 patients with soft tissue sarcoma. *Annals of Surgery*, *260*, 416–422.

Broad, K., Walker, S. A., Davidovich, I., Witwer, K., Talmon, Y., & Wolfram, J. (2023). Unraveling multilayered extracellular vesicles: Speculation on cause. *Journal of Extracellular Vesicles*, *12*, e12309.

Calo, A., Reguera, D., Oncins, G., Persuy, M. A., Sanz, G., Lobasso, S., Corcelli, A., Pajot-Augy, E., & Gomila, G. (2014). Force measurements on natural membrane nanovesicles reveal a composition-independent, high Young's modulus. *Nanoscale*, *6*, 2275–2285.

Carman, P. C. (1937). Fluid flow through granular beds. *Transactions, Institution of Chemical Engineers*, *15*, 15–166.

Carman, P. C. (1997). Fluid flow through granular beds. *Chemical Engineering Research and Design*, *75*, S32–S48.

Casadei, L., Calore, F., Braggio, D. A., Zewdu, A., Deshmukh, A. A., Fadda, P., Lopez, G., Wabitsch, M., Song, C., Leight, J. L., Grignol, V. P., Lev, D., Croce, C. M., & Pollock, R. E. (2019). MDM2 derived from dedifferentiated liposarcoma extracellular vesicles induces MMP2 production from preadipocytes. *Cancer Research*, *79*, 4911–4922.

Casadei, L., Choudhury, A., Sarchet, P., Sundaram, P. M., Lopez, G., Braggio, D., Balakirsky, G., Pollock, R., & Prakash, S. (2021). Cross-flow microfiltration for isolation, selective capture and release of liposarcoma extracellular vesicles. *Journal of Extracellular Vesicles*, *10*, e12062.

Casadei, L., & Pollock, R. E. (2020). Extracellular vesicle cross-talk in the liposarcoma microenvironment. *Cancer Letters*, *487*, 27–33.

Casadei, L., Sarchet, P., de Faria, F. C. C., Calore, F., Nigita, G., Tahara, S., Cascione, L., Wabitsch, M., Hornicek, F. J., Grignol, V., Croce, C. M., & Pollock, R. E. (2022). In situ hybridization to detect DNA amplification in extracellular vesicles. *Journal of Extracellular Vesicles*, *11*, e12251.

Castillo, J., Bernard, V., San Lucas, F. A., Allenson, K., Capello, M., Kim, D. U., Gascoyne, P., Mulu, F. C., Stephens, B. M., Huang, J., Wang, H., Momin, A. A., Jacamo, R. O., Katz, M., Wolff, R., Javle, M., Varadhachary, G., Wistuba, I. I., Hanash, S., … Alvarez, H. (2018). Surfaceome profiling enables isolation of cancer-specific exosomal cargo in liquid biopsies from pancreatic cancer patients. *Annals of Oncology*, *29*, 223–229.

Cedervall, T., Lynch, I., Lindman, S., Berggård, T., Thulin, E., Nilsson, H., Dawson, K. A., & Linse, S. (2007). Understanding the nanoparticle-protein corona using methods to quantify exchange rates and affinities of proteins for nanoparticles. *Proceedings of the National Academy of Sciences of the United States of America*, *104*, 2050–2055.

Chang, Y. R., Raghunathan, V. K., Garland, S. P., Morgan, J. T., Russell, P., & Murphy, C. J. (2014). Automated AFM force curve analysis for determining elastic modulus of biomaterials and biological samples. *Journal of the Mechanical Behavior of Biomedical Materials*, *37*, 209–218.

Chernyshev, V. S., Chuprov-Netochin, R. N., Tsydenzhapova, E., Svirshchevskaya, E. V., Poltavtseva, R. A., Merdalimova, A., Yashchenok, A., Keshelava, A., Sorokin, K., Keshelava, V., Sukhikh, G. T., Gorin, D., Leonov, S., & Skliar, M. (2022). Asymmetric depth-filtration: A versatile and scalable method for high-yield isolation of extracellular vesicles with low contamination. *Journal of Extracellular Vesicles*, *11*, e12256.

Chng, C. P., Sadovsky, Y., Hsia, K. J., & Huang, C. J. (2021). Curvature-regulated lipid membrane softening of nano-vesicles. *Extreme Mechanics Letters*, *43*, 101174.

Comfort, N., Cai, K., Bloomquist, T. R., Strait, M. D., Ferrante A. W., Jr., & Baccarelli, A. A. (2021). Nanoparticle tracking analysis for the quantification and size determination of extracellular vesicles. *Journal of Visualized Experiments: JoVE*, *169*, 62447. https://doi.org/10.3791/62447

Darcy, H. (1856). Les fontaines publiques de la ville de Dijon: Exposition et application des principes a suivre et des formules a employer dans les questions de distribution d'eau; ouvrage terminé par un appendice relatif aux fournitures d'eau de plusieurs villes au filtrage des eaux et a la fabrication des tuyaux de fonte, de plomb, de tole et de bitume. Victor Dalmont, Libraire des Corps imperiaux des ponts et chaussées et des mines.

de Meyer, F., & Smit, B. (2009). Effect of cholesterol on the structure of a phospholipid bilayer. *Proceedings of the National Academy of Sciences of the United States of America*, *106*, 3654–3658.

Dehghani, M., Lucas, K., Flax, J., McGrath, J., & Gaborski, T. (2019). Tangential flow microfluidics for the capture and release of nanoparticles and extracellular vesicles on conventional and ultrathin membranes. *Advanced Materials Technologies*, *4*(11), 1900539.

Dixson, A. C., Dawson, T. R., Di Vizio, D., & Weaver, A. M. (2023). Context-specific regulation of extracellular vesicle biogenesis and cargo selection. *Nature Reviews Molecular Cell Biology*, *24*(7), 454–476.

Durcin, M., Fleury, A., Taillebois, E., Hilairet, G., Krupova, Z., Henry, C., Truchet, S., Trotzmuller, M., Kofeler, H., Mabilleau, G., Hue, O., Andriantsitohaina, R., Martin, P., & Lay, S. Le (2017). Characterisation of adipocyte-derived extracellular vesicle subtypes identifies distinct protein and lipid signatures for large and small extracellular vesicles. *Journal of Extracellular Vesicles*, *6*(1), 1305677.

Durlofsky, L., & Brady, J. F. (1987). Analysis of the Brinkman equation as a model for flow in porous-media. *Physics of Fluids*, *30*, 3329–3341.

Elzanowska, J., Semira, C., & Costa-Silva, B. (2021). DNA in extracellular vesicles: Biological and clinical aspects. *Molecular Oncology*, *15*, 1701–1714.

Fay, M. P., & Proschan, M. A. (2010). Wilcoxon-Mann-Whitney or t-test? On assumptions for hypothesis tests and multiple interpretations of decision rules. *Statistics Surveys*, *4*, 1–39.

Gamboa, A. C., Gronchi, A., & Cardona, K. (2020). Soft-tissue sarcoma in adults: An update on the current state of histiotype-specific management in an era of personalized medicine. *CA: A Cancer Journal for Clinicians*, *70*, 200–229.

Hallal, S., Tuzesi, A., Grau, G. E., Buckland, M. E., & Alexander, K. L. (2022). Understanding the extracellular vesicle surface for clinical molecular biology. *Journal of Extracellular Vesicles*, *11*, e12260.

Haraszti, R. A., Didiot, M. C., Sapp, E., Leszyk, J., Shaffer, S. A., Rockwell, H. E., Gao, F., Narain, N. R., DiFiglia, M., Kiebish, M. A., Aronin, N., & Khvorova, A. (2016). High-resolution proteomic and lipidomic analysis of exosomes and microvesicles from different cell sources. *Journal of Extracellular Vesicles*, *5*, 32570.

Helfrich, W. (1986). Size distributions of vesicles - the role of the effective rigidity of membranes. *Journal of Physics-Paris*, *47*, 321–329.

Huang, C. J., Quinn, D., Sadovsky, Y., Suresh, S., & Hsia, K. J. (2017). Formation and size distribution of self-assembled vesicles. *Proceedings of the National Academy of Sciences of the United States of America*, *114*, 2910–2915.

Hung, W. C., Lee, M. T., Chen, F. Y., & Huang, H. W. (2007). The condensing effect of cholesterol in lipid bilayers. *Biophysical Journal*, *92*, 3960–3967.

Jung, D., Shin, S., Kang, S.-M., Jung, I., Ryu, S., Noh, S., Choi, S.-J., Jeong, J., Lee, B. Y., Kim, K.-S., Kim, C. S., Yoon, J. H., Lee, C.-H., Bucher, F., Kim, Y.-N., Im, S.-H., Song, B.-J., Yea, K., & Baek, M.-C. (2022). Reprogramming of T cell-derived small extracellular vesicles using IL2 surface engineering induces potent anti-cancer effects through miRNA delivery. *Journal of Extracellular Vesicles*, *11*, 12287.

Kalluri, R., & LeBleu, V. S. (2020). The biology, function, and biomedical applications of exosomes. *Science*, *367*, eaau6977.

Karavasilis, V., Seddon, B. M., Ashley, S., Al-Muderis, O., Fisher, C., & Judson, I. (2008). Significant clinical benefit of first-line palliative chemotherapy in advanced soft-tissue sarcoma - Retrospective analysis and identification of prognostic factors in 488 patients. *Cancer-Journal of American Cancer Society*, *112*, 1585–1591.

Kesimer, M., Scull, M., Brighton, B., DeMaria, G., Burns, K., O'Neal, W., Pickles, R. J., & Sheehan, J. K. (2009). Characterization of exosome-like vesicles released from human tracheobronchial ciliated epithelium: a possible role in innate defense. *FASEB Journal*, *23*, 1858–1868.

Kozeny, J. (1927). Ueber kapillare Leitung des Wassers im Boden. *Sitzungsberichte der Akademie der Wissenschaften in Wien*, *136*(2a), 271–306.

Lane, R., Simon, T., Vintu, M., Solkin, B., Koch, B., Stewart, N., Benstead-Hume, G., Pearl, F. M. G., Critchley, G., Stebbing, J., & Giamas, G. (2019). Cell-derived extracellular vesicles can be used as a biomarker reservoir for glioblastoma tumor subtyping. *Communications Biology*, *2*, 315.

Laney, D. E., Garcia, R. A., Parsons, S. M., & Hansma, H. G. (1997). Changes in the elastic properties of cholinergic synaptic vesicles as measured by atomic force microscopy. *Biophysical Journal*, *72*, 806–813.

Lazaro-Ibanez, E., Lasser, C., Shelke, G. V., Crescitelli, R., Jang, S. C., Cvjetkovic, A., Garcia-Rodriguez, A., & Lotvall, J. (2019). DNA analysis of low- and high-density fractions defines heterogeneous subpopulations of small extracellular vesicles based on their DNA cargo and topology. *Journal of Extracellular Vesicles*, *8*, 1656993.

LeClaire, M., Gimzewski, J., & Sharma, S. (2021). A review of the biomechanical properties of single extracellular vesicles. *Nano Select*, *2*, 1–15.

LeClaire, M., Wohlschlegel, J. A., Chang, H., Wadehra, M., Yu, W. B., Rao, J. Y., Elashoff, D., Gimzewski, J. K., & Sharma, S. (2021). Nanoscale extracellular vesicles carry the mechanobiology signatures of breast cancer cells. *ACS Applied Nano Materials*, *4*, 9876–9885.

Lee, A. T. J., Thway, K., Huang, P. H., & Jones, R. L. (2018). Clinical and molecular spectrum of liposarcoma. *Journal of Clinical Oncology*, *36*, 151–159.

Li, G., Chen, T., Dahlman, J., Eniola-Adefeso, L., Ghiran, I. C., Kurre, P., Lam, W. A., Lang, J. K., Marbán, E., Martín, P., Momma, S., Moos, M., Nelson, D. J., Raffai, R. L., Ren, X., Sluijter, J. P. G., Stott, S. L., Vunjak-Novakovic, G., Walker, N. D., … Sundd, P. (2023). Current challenges and future directions for engineering extracellular vesicles for heart, lung, blood and sleep diseases. *Journal of Extracellular Vesicles*, *12*, 12305.

Liang, L. G., Sheng, Y. F., Zhou, S., Inci, F., Li, L., Demirci, U., & Wang, S. (2017). An integrated double-filtration microfluidic device for detection of extracellular vesicles from urine for bladder cancer diagnosis. *Methods in Molecular Biology*, *1660*, 355–364.

Liu, D., Zhang, Z. H., Wang, R., & Hu, J. L. (2022). Stability and deformation of vesicles in a cylindrical flow. *Langmuir*, *38*, 629–637.

ŁUkasiewicz, S. A. (1971). The Equations of the technical theory of shells with the effect of transverse shear deformation. *Quarterly of Applied Mathematics*, *28*, 489–497.

Mathieu, M., Martin-Jaular, L., Lavieu, G., & Théry, C. (2019). Specificities of secretion and uptake of exosomes and other extracellular vesicles for cell-to-cell communication. *Nature Cell Biology*, *21*, 9–17.

Merchant, M. L., Powell, D. W., Wilkey, D. W., Cummins, T. D., Deegens, J. K., Rood, I. M., McAfee, K. J., Fleischer, C., Klein, E., & Klein, J. B. (2010). Microfiltration isolation of human urinary exosomes for characterization by MS. *Proteomics Clinical Applications*, *4*, 84–96.

Mietke, A., Otto, O., Girardo, S., Rosendahl, P., Taubenberger, A., Golfier, S., Ulbricht, E., Aland, S., Guck, J., & Fischer-Friedrich, E. (2015). Extracting cell stiffness from real-time deformability cytometry: Theory and experiment. *Biophysical Journal*, *109*, 2023–2036.

Mihaly, J., Deak, R., Szigyarto, I. C., Bota, A., Beke-Somfai, T., & Varga, Z. (2017). Characterization of extracellular vesicles by IR spectroscopy: Fast and simple classification based on amide and CH stretching vibrations. *Biochim Biophys Acta Biomembr*, *1859*, 459–466.

Molina-Garcia, A. D. (1999). *Hydrostatic pressure in ultracentrifugation* (pp. 57–61). Springer Berlin Heidelberg.

Morandi, M. I., Busko, P., Ozer-Partuk, E., Khan, S., Zarfati, G., Elbaz-Alon, Y., Abou Karam, P., Napso Shogan, T., Ginini, L., Gil, Z., Regev-Rudzki, N., & Avinoam, O. (2022). Extracellular vesicle fusion visualized by cryo-electron microscopy. *PNAS Nexus*, *1*, pgac156.

Morshed, A., Karawdeniya, B. I., Bandara, Y., Kim, M. J., & Dutta, P. (2020). Mechanical characterization of vesicles and cells: A review. *Electrophoresis*, *41*, 449–470.

Nguyen, V. V. T., Ye, S., Gkouzioti, V., van Wolferen, M. E., Yengej, F. Y., Melkert, D., Siti, S., de Jong, B., Besseling, P. J., Spee, B., van der Laan, L. J. W., Horland, R., Verhaar, M. C., & van Balkom, B. W. M. (2022). A human kidney and liver organoid-based multi-organ-on-a-chip model to study the therapeutic effects and biodistribution of mesenchymal stromal cell-derived extracellular vesicles. *Journal of Extracellular Vesicles*, *11*, 12280.

Paolini, L., Federici, S., Consoli, G., Arceri, D., Radeghieri, A., Alessandri, I., & Bergese, P. (2020). Fourier-transform Infrared (FT-IR) spectroscopy fingerprints subpopulations of extracellular vesicles of different sizes and cellular origin. *Journal of Extracellular Vesicles*, *9*, 1741174.

Parisse, P., Rago, I., Severino, L. U., Perissinotto, F., Ambrosetti, E., Paoletti, P., Ricci, M., Beltrami, A. P., Cesselli, D., & Casalis, L. (2017). Atomic force microscopy analysis of extracellular vesicles. *European Biophysics Journal*, *46*, 813–820.

Peng, T., Zhang, P., Liu, J., Nguyen, T., Bolshakov, S., Belousov, R., Young, E. D., Wang, X., Brewer, K., Lopez-Terrada, D. H., Oliveira, A. M., Lazar, A. J., & Lev, D. (2011). An experimental model for the study of well-differentiated and dedifferentiated liposarcoma; deregulation of targetable tyrosine kinase receptors. *Laboratory Investigation*, *91*, 392–403.

Perissinotto, F., Rondelli, V., Senigagliesi, B., Brocca, P., Almásy, L., Bottyán, L., Merkel, D. G., Amenitsch, H., Sartori, B., Pachler, K., Mayr, M., Gimona, M., Rohde, E., Casalis, L., & Parisse, P. (2021). Structural insights into fusion mechanisms of small extracellular vesicles with model plasma membranes. *Nanoscale*, *13*, 5224–5233.

Phillips, W., Willms, E., & Hill, A. F. (2021). Understanding extracellular vesicle and nanoparticle heterogeneity: Novel methods and considerations. *Proteomics*, *21*, e2000118.

Rangharajan, K. K., Fuest, M., Conlisk, A. T., & Prakash, S. (2016). Transport of multicomponent, multivalent electrolyte solutions across nanocapillaries. *Microfluidics and Nanofluidics*, *20*, 54.

Ridolfi, A., Brucale, M., Montis, C., Caselli, L., Paolini, L., Borup, A., Boysen, A. T., Loria, F., van Herwijnen, M. J. C., Kleinjan, M., Nejsum, P., Zarovni, N., Wauben, M. H. M., Berti, D., Bergese, P., & Valle, F. (2020). AFM-Based High-Throughput Nanomechanical Screening of Single Extracellular Vesicles. *Analytical Chemistry*, *92*, 10274–10282.

Ridolfi, A., Conti, L., Brucale, M., Frigerio, R., Cardellini, J., Musicò, A., Romano, M., Zendrini, A., Polito, L., Bergamaschi, G., Gori, A., Montis, C., Panella, S., Barile, L., Berti, D., Radeghieri, A., Bergese, P., Cretich, M., & Valle, F. (2023). Particle profiling of EV-lipoprotein mixtures by AFM nanomechanical imaging. *Journal of Extracellular Vesicles*, *12*, 12349.

Rikkert, L. G., Nieuwland, R., Terstappen, L., & Coumans, F. A. W. (2019). Quality of extracellular vesicle images by transmission electron microscopy is operator and protocol dependent. *Journal of Extracellular Vesicles*, *8*, 1555419.

Rodriguez-Quijada, C., & Dahl, J. B. (2021). Non-contact microfluidic mechanical property measurements of single apoptotic bodies. *BBA General Subjects*, *1865*, 129657.

Roos, W. H., Bruinsma, R., & Wuite, G. J. L. (2010). Physical virology. *Nature Physics*, *6*, 733–743.

Royo, F., Gil-Carton, D., Gonzalez, E., Mleczko, J., Palomo, L., Perez-Cormenzana, M., Mayo, R., Alonso, C., & Falcon-Perez, J. M. (2019). Differences in the metabolite composition and mechanical properties of extracellular vesicles secreted by hepatic cellular models. *Journal of Extracellular Vesicles*, *8*, 1575678.

Sanders, J. L. (1963). Nonlinear theories for thin shells. *Quarterly of Applied Mathematics*, *21*, 21–36.

Seide, P., & Nordgren, R. P. (1976). Small elastic deformations of thin shells. *Journal of Applied Mechanics*, *43*, 702–702.

Singh, P. K., Patel, A., Kaffenes, A., Hord, C., Kesterson, D., & Prakash, S. (2022). Microfluidic approaches and methods enabling extracellular vesicle isolation for cancer diagnostics. *Micromachines*, *13*, 139.

Smith, B. C. (2003). *Quantitative spectroscopy: Theory and practice*. Elsevier.

Sorkin, R., Huisjes, R., Boskovic, F., Vorselen, D., Pignatelli, S., Ofir-Birin, Y., Leal, J. K. F., Schiller, J., Mullick, D., Roos, W. H., Bosman, G., Regev-Rudzki, N., Schiffelers, R. M., & Wuite, G. J. L. (2018). Nanomechanics of extracellular vesicles reveals vesiculation pathways. *Small*, *14*, e1801650.

Tan, M. C. B., Brennan, M. F., Kuk, D., Agaram, N. P., Antonescu, C. R., Qin, L.-X., Moraco, N., Crago, A. M., & Singer, S. (2016). Histology-based classification predicts pattern of recurrence and improves risk stratification in primary retroperitoneal sarcoma. *Annals of Surgery*, *263*, 593–600.

Tang, X. Y., Shi, X. H., Gan, Y., & Yi, X. (2020). Nanomechanical characterization of pressurized elastic fluid nanovesicles using indentation analysis. *Extreme Mechanics Letters*, *34*, 100613.

Tao, S.-C., & Guo, S.-C. (2020). Role of extracellular vesicles in tumour microenvironment. *Cell Communication and Signaling*, *18*, 163.

Teng, F., & Fussenegger, M. (2021). Shedding light on extracellular vesicle biogenesis and bioengineering. *Advanced Science*, *8*, 2003505.

Tertel, T., Tomić, S., Đokić, J., Radojević, D., Stevanović, D., Ilić, N., Giebel, B., & Kosanović, M. (2022). Serum-derived extracellular vesicles: Novel biomarkers reflecting the disease severity of COVID-19 patients. *Journal of Extracellular Vesicles*, *11*, e12257.

Thway, K. (2009). Pathology of soft tissue sarcomas. *Clinical Oncology*, *21*, 695–705.

Timoshenko, S. P., & Woinowsky-krieger, S. (1959). Theory of Plates and Shells. 2nd Edition, McGraw-Hill, New York.

Tóth, E., Turiák, L., Visnovitz, T., Cserép, C., Mázló, A., Sódar, B. W., Försönits, A. I., Petővári, G., Sebestyén, A., Komlósi, Z., Drahos, L., Kittel, Á., Nagy, G., Bácsi, A., Dénes, Á., Gho, Y. S., Szabó-Taylor, K., & Buzás, E. I. (2021). Formation of a protein corona on the surface of extracellular vesicles in blood plasma. *Journal of Extracellular Vesicles*, *10*, e12140.

Vagner, T., Chin, A., Mariscal, J., Bannykh, S., Engman, D. M., & Di Vizio, D. (2019). Protein composition reflects extracellular vesicle heterogeneity. *Proteomics*, *19*, 1800167.

van Niel, G., Carter, D. R. F., Clayton, A., Lambert, D. W., Raposo, G., & Vader, P. (2022). Challenges and directions in studying cell–cell communication by extracellular vesicles. *Nature Reviews Molecular Cell Biology*, *23*, 369–382.

van Niel, G., D'Angelo, G., & Raposo, G. (2018). Shedding light on the cell biology of extracellular vesicles. *Nature Reviews Molecular Cell Biology*, *19*, 213–228.

Vitarelli, M. J., Jr., Prakash, S., & Talaga, D. S. (2011). Determining nanocapillary geometry from electrochemical impedance spectroscopy using a variable topology network circuit model. *Analytical Chemistry*, *83*, 533–541.

Vorselen, D., MacKintosh, F. C., Roos, W. H., & Wuite, G. J. L. (2017). Competition between bending and internal pressure governs the mechanics of fluid nanovesicles. *ACS Nano*, *11*, 2628–2636.

Wang, Z., Wu, H. J., Fine, D., Schmulen, J., Hu, Y., Godin, B., Zhang, J. X., & Liu, X. (2013). Ciliated micropillars for the microfluidic-based isolation of nanoscale lipid vesicles. *Lab Chip*, *13*, 2879–2882.

Waugh, R. E., & Song, J. B. (1991). Measurements of membrane bending stiffness - Contributions from intrinsic monolayer stiffness and monolayer coupling. *Periodicum Biologorum*, *93*, 217–222.

Welsh, J. A., Goberdhan, D. C. I., O'Driscoll, L., Buzas, E. I., Blenkiron, C., Bussolati, B., Cai, H., Di Vizio, D., Driedonks, T. A. P., Erdbrügger, U., Falcon-Perez, J. M., Fu, Q. L., Hill, A. F., Lenassi, M., Lim, S. K., Mahoney, M. G., Mohanty, S., Möller, A., Nieuwland, R., … Witwer, K. W. (2024). Minimal information for studies of extracellular vesicles (MISEV2023): From basic to advanced approaches. *Journal of Extracellular Vesicles*, *13*, e12404.

White, F. M. (2011). *Fluid mechanics*. McGraw- Hill.

Whitehead, B., Wu, L., Hvam, M. L., Aslan, H., Dong, M., Dyrskjot, L., Ostenfeld, M. S., Moghimi, S. M., & Howard, K. A. (2015). Tumour exosomes display differential mechanical and complement activation properties dependent on malignant state: implications in endothelial leakiness. *Journal of Extracellular Vesicles*, *4*, 29685.

Wiklander, O. P. B., Brennan, M. Á., Lötvall, J., Breakefield, X. O., & EL Andaloussi, S. (2019). Advances in therapeutic applications of extracellular vesicles. *Science Translational Medicine*, *11*, eaav8521.

Wolf, M., Poupardin, R. W., Ebner-Peking, P., Andrade, A. C., Blöchl, C., Obermayer, A., Gomes, F. G., Vari, B., Maeding, N., Eminger, E., Binder, H. M., Raninger, A. M., Hochmann, S., Brachtl, G., Spittler, A., Heuser, T., Ofir, R., Huber, C. G., Aberman, Z., … Strunk, D. (2022). A functional corona around extracellular vesicles enhances angiogenesis, skin regeneration and immunomodulation. *Journal of Extracellular Vesicles*, *11*, e12207.

Yang, M., Walker, S. A., de Leon, J. S. A. D., Davidovich, I., Broad, K., Talmon, Y., Borges, C. R., & Wolfram, J. (2022). Extracellular vesicle glucose transporter-1 and glycan features in monocyte-endothelial inflammatory interactions. *Nanomedicine: Nanotechnology*, *42*, 102515.

Yuana, Y., Böing, A. N., Grootemaat, A. E., van der Pol, E., Hau, C. M., Cizmar, P., Buhr, E., Sturk, A., & Nieuwland, R. (2015). Handling and storage of human body fluids for analysis of extracellular vesicles. *Journal of Extracellular Vesicles*, *4*, 29260.

Yuana, Y., Koning, R. I., Kuil, M. E., Rensen, P. C. N., Koster, A. J., Bertina, R. M., & Osanto, S. (2013). Cryo-electron microscopy of extracellular vesicles in fresh plasma. *Journal of Extracellular Vesicles*, *2*, 21494.

Yurtsever, A., Yoshida, T., Badami Behjat, A., Araki, Y., Hanayama, R., & Fukuma, T. (2021). Structural and mechanical characteristics of exosomes from osteosarcoma cells explored by 3D-atomic force microscopy. *Nanoscale*, *13*, 6661–6677.

Zhang, H. Y., Freitas, D., Kim, H. S., Fabijanic, K., Li, Z., Chen, H. Y., Mark, M. T., Molina, H., Martin, A. B., Bojmar, L., Fang, J., Rampersaud, S., Hoshino, A., Matei, I., Kenific, C. M., Nakajima, M., Mutvei, A. P., Sansone, P., Buehring, W., … Lyden, D. (2018). Identification of distinct nanoparticles and subsets of extracellular vesicles by asymmetric flow field-flow fractionation. *Nature Cell Biology*, *20*, 332–343.

Zhang, Z., Liu, X., Yang, X., Jiang, Y., Li, A., Cong, J., Li, Y., Xie, Q., Xu, C., & Liu, D. (2023). Identification of faecal extracellular vesicles as novel biomarkers for the non-invasive diagnosis and prognosis of colorectal cancer. *Journal of Extracellular Vesicles*, *12*, 12300.

SUPPORTING INFORMATION

Additional supporting information can be found online in the Supporting Information section at the end of this article.

How to cite this article: Singh, P. K., Sarchet, P., Hord, C., Casadei, L., Pollock, R., & Prakash, S. (2024). Mechanical property estimation of sarcoma-relevant extracellular vesicles using transmission electron microscopy. *Journal of Extracellular Biology*, *3*, e158. https://doi.org/10.1002/jex2.158